


**Please cite the Published Version**

Wang, K, Ma, X, Bai, Wei , Lin, Z and Li, Y (2021) Numerical simulation of water entry of a symmetric/asymmetric wedge into waves using OpenFOAM. Ocean Engineering, 227. ISSN 0029-8018

**DOI:** <https://doi.org/10.1016/j.oceaneng.2021.108923>

**Publisher:** Elsevier

**Version:** Accepted Version

**Downloaded from:** <https://e-space.mmu.ac.uk/627427/>

**Usage rights:**  [Creative Commons: Attribution-Noncommercial-No Derivative Works 4.0](#)

**Additional Information:** Author accepted manuscript published by and copyright Elsevier.

**Enquiries:**

If you have questions about this document, contact [openresearch@mmu.ac.uk](mailto:openresearch@mmu.ac.uk). Please include the URL of the record in e-space. If you believe that your, or a third party's rights have been compromised through this document please see our Take Down policy (available from <https://www.mmu.ac.uk/library/using-the-library/policies-and-guidelines>)

# Numerical simulation of water entry of a symmetric/asymmetric wedge into waves using OpenFOAM

Kai Wang<sup>1</sup>, Xin Ma<sup>1\*</sup>, Wei Bai<sup>2</sup>, Zaibin Lin<sup>2</sup>, Yibin Li<sup>1</sup>

<sup>1</sup>School of Control Science and Engineering, Shandong University, Shandong, CHINA

<sup>2</sup>Department of Computing and Mathematics, Manchester Metropolitan University, Manchester,  
M1 5GD, United Kingdom

\*This work was supported by the Joint Funds of the National Natural Science Foundation of China-Shandong  
Province [grant numbers.U1706228]

\*Corresponding Author: [maxin@sdu.edu.cn](mailto:maxin@sdu.edu.cn)

Full postal address: 17923 Jingshi Road. Jinan 250061, Shandong, P. R. China

## **Abstract:**

This paper presents a dynamic overset mesh based two-dimensional Numerical Wave Tank (NWT) model to study the water entry of a wedge into water waves in the process of offshore lowering. The NWT model is developed by integrating an incompressible multiphase flow solver on the dynamic overset mesh and a wave generation library in OpenFOAM. Numerical results of water entry of a symmetric/asymmetric wedge into the still water are presented to validate the NWT model by comparing with the published data. A series of numerical simulations of water entry of a symmetrical/asymmetrical wedge into regular waves are carried out, and the pressure

coefficients, total force and free surface profiles are presented. Based on the parametric study on the water entry of a wedge into waves, the influence of wave amplitude, water entry velocity, and water entry location (wave peak, wave trough, cross point with the still water level) is analyzed. The numerical solutions provide the fundamentals for the further research on the safe control of water entry of payloads during the offshore installation.

**Keywords:** Numerical wave tank, Offshore crane, OpenFOAM, Water entry, Wedge

## 1. Introduction

With ever-increasing marine exploration and subsea resource exploitation, offshore cranes which are mounted on vessels and carry out lifting/lowering have been widely used in ocean engineering. While working on the sea, offshore cranes suffer from the persistent disturbances induced by ocean waves. During lifting or lowering, the payloads may be subjected to hydrodynamic forces that vary significantly during the water entry or exit, which could cause payload damages or cable breaks, and further lead to accidents and impair the safety of life and property (Driscoll et al., 2000; Hover et al., 1994; Ma et al., 2018). A modelling tool that can predict the hydrodynamic loads on payloads in the process of water entry in waves is vitally important for lowering payloads in the sea safely and efficiently.

Water entry is a complex nonlinear problem. Water entry of a wedge has been

extensively studied for various applications such as ship advancing in rough sea and offshore structure design. Based on the theoretical analysis of the similarity flow induced by the wedge entry, an analytical solution of a nonlinear singular integral equation was developed for the water entry of a symmetrical wedge into the calm water (Dobrovolskaya, 1969) under the assumption of inviscid and incompressible fluid. A self-similar solution of water entry of an asymmetric wedge into the calm water with a constant vertical velocity was also derived in (Semenov and Iafrati, 2006). These analytical methods are limited to wedges or objects with a simple geometry entering into the calm water.

Potential flow theory based numerical methods has been developed for the investigation of water entry. For example, the boundary element method (BEM) was used for the water entry of a symmetric wedge (Zhao and Faltinsen, 1993) and an asymmetric body with a constant vertical speed. Oblique water entry of an asymmetrical wedge was solved by combining Wu et al. (2004)'s BEM with an analytical solution of the integral equation along the fluid boundary (Xu et al., 2008). By adding the inclination angle, Barjasteh et al. (2016) experimentally studied the water entry of asymmetric wedge and recorded the time histories of impact pressure and body acceleration. Sun et al. (2015) analyzed the wedge entering waves with the gravity effect. However, with the assumption that the flow is inviscid and flow irrotational, it is challenging for the potential flow theory to capture the nonlinear free surface accurately when the wave breaking occurs. Computation fluid dynamics (CFD) based on the Navier-Stokes equations can deal with this difficulty. Various CFD-based

numerical models have been considered for the water entry of a symmetric/asymmetric wedge, such as the volume of fluid (VOF) in (Gu et al., 2014; Kleefsman et al., 2005; Tassin et al., 2013), the smoothed particle hydrodynamics (SPH) in (Oger et al., 2006; Panciroli et al., 2012), and the constrained interpolation profile (CIP) in (Hu et al., 2018; Wen and Qiu, 2015; Yang and Qiu, 2012).

OpenFOAM, a free open-source C++ toolbox for the development of a customized numerical solver based on CFD, has been applied in coastal and offshore engineering recently. The performance of OpenFOAM for water entry was evaluated in (Chen et al., 2019; Ma and Qian, 2018; Ma et al., 2018). Among different numerical techniques, the overset mesh consists of multiple sub-grids that transfer information through interpolation and are independent from each other in the modeling. It can keep the good quality of the computational mesh for complex geometric figurations, which is especially suitable for the simulation of large amplitude motions (Chan, 2009; Chen et al., 2019). In recent years, many researchers have been focusing on the overset mesh technique in OpenFOAM (Chandar et al., 2018; Shen et al., 2015; Wang et al., 2017). In particular, Ma et al. (2018) used the overset mesh to simulate the process of wedge entering the calm water.

In the realistic offshore environment, lifting or lowering payloads on a crane ship is usually carried out under wave conditions. Therefore, water entry of a wedge into waves needs to be simulated accurately for assessing the risk of cargo lowering into waves with the constant velocity. However, the problem of the wedge entering vertically into waves is much more complicated than entering into the calm water,

because it is subjected to more complex hydrodynamic forces which cause the wedge to sway and turn over. The incident wave makes the problem more nonlinear and the result is no longer self-similar even for a short time in the early stage of water-entry. Furthermore, the solution of the time-varying free profile is more complex. Cheng et al. (2018) and Sun et al. (2015) studied the water entry of a wedge into waves, using the potential flow theory, which does not account for the viscosity and vorticity of the fluid.

Most wedge water-entry studies focus on ship slamming to predict the critical hydrodynamic loadings and assess the potential risks to ships at the moment of entering the water. Zhao and Faltinsen (1993) calculated the impact pressures on the wedge entering the calm water. Sun et al. (2015) and Cheng et al. (2018) calculated the pressure distribution and free surface of the wedge entering a wave. Their work studied the wedge that has infinite volume with dimensionless processing, rather than the wedge of the finite volume that is of more importance in offshore crane engineering. The change of hydrodynamic force on a wedge in the whole wave-entry duration from touching the water surface to immersing into the water was not presented in their studies. Different from their studies, the topic in the paper concerns the hydrodynamic force changes of symmetric/asymmetric wedges that have finite volumes entering into waves in the whole duration of water entry. The contributions of the paper are as follows: (1) Aiming at safe hoisting operation of crane vessels, wave-entry of wedges that have finite volumes in the whole duration of entering wave from touching the water surface to submerging into the wave is studied. Detailed results of the free surface and the pressure distribution are provided to analyze the influence of wave parameter, entry

velocity, and entry location on the hydrodynamic force of symmetric/asymmetric wedges that have finite volumes. To the best of our knowledge, it is the first work on the hydrodynamic force of wedges that have finite volumes entering into waves for the whole duration of water-entry. (2) Two-dimensional overset-mesh based numerical wave tank (NWT) is established in OpenFOAM, which solves the Navier–Stokes equations, and is able to generate the nonlinear phenomena caused by the viscosity and vorticity of the fluid with the complex water surface. (3) The motion solver in OpenFOAM is modified to preset the payload's trajectory, which can make the wedge remain stable before the several wave cycles are generated and fall into the desired location in the wave accurately.

The rest of the paper is organized as follows. The numerical model is given in Section 2. In Section 3, the 2D NWT model is validated by comparing the results of water entry of wedges into the calm water with the published data. A series of simulations of the water entry of a symmetric/asymmetric wedge into regular waves are carried out in Section 4, where the influences of incident wave amplitude, entry velocity, and entry location are analyzed, followed by the main conclusions drawn in Section 5.

## 2. Numerical model

### 2.1 Governing equations

In order to simulate the water entry of a wedge in waves, two Cartesian coordinate frames are defined. As shown in Fig. 1,  $(x_g O_g z_g)$  is the space fixed frame, where  $O_g$  is the origin fixed at the left bottom of the numerical tank, with the  $x$  axis parallel to

the free surface and  $z$  axis pointing vertically upwards.  $xoz$  is the frame fixed to the wedge, where  $o$  is defined at the wedge vertex. These two coordinate frames are parallel when the wedge is at its initial position. The two deadrise angles are defined as  $\gamma_1$  and  $\gamma_2$  respectively, which have the same values for a symmetric wedge. The velocity of the wedge consists of a horizontal velocity component  $u$  and a downward vertical velocity component  $v$ .

The fluid flow in this water entry problem can be described by the continuity equation:

$$\frac{\partial \rho}{\partial t} + \nabla \cdot (\rho \mathbf{U}) = 0, \quad (1)$$

where  $\mathbf{U}$  is the fluid velocity,  $\rho$  the fluid density and  $t$  the time, and the Navier-Stokes equations:

$$\frac{\partial \rho \mathbf{U}}{\partial t} + \nabla \cdot (\rho \mathbf{U} \mathbf{U}) - \nabla \cdot (\mu \nabla \mathbf{U}) = -g \cdot x \nabla \rho - \nabla p_d, \quad (2)$$

where  $p_d = p - \rho g \cdot x$  is the dynamic pressure,  $p$  the total pressure,  $\mu$  the dynamic viscosity,  $x$  the position vectors, and  $g$  the gravitational acceleration.

The free surface is solved by the volume of fluid (VOF) method (Hirt and Nichols, 1981). In VOF, the water volume fraction is defined as  $\alpha \in [0, 1]$ . Considering an air-liquid two-phase system, if the grid element is filled with liquid,  $\alpha = 1$ ; if the cell is filled with air,  $\alpha = 0$ . Otherwise, the value of  $\alpha$  is between 0 and 1, and the cell is at the free surface. Hence the fluid density and the dynamic viscosity in each cell are calculated with the equations:

$$\rho = \alpha \rho_{\text{water}} + (1 - \alpha) \rho_{\text{air}}, \quad (3)$$



$$\mu = \alpha\mu_{\text{water}} + (1-\alpha)\mu_{\text{air}}, \quad (4)$$

where  $\rho_{\text{water}}$  and  $\rho_{\text{air}}$  are the density of water and air respectively,  $\mu_{\text{water}}$  and  $\mu_{\text{air}}$  are the viscosity of water and air respectively. Hereby, the water volume fraction  $\alpha$  can be solved by the volume fraction transport equation:

$$\frac{\partial \alpha}{\partial t} + \nabla \cdot \mathbf{U} \alpha + \nabla \cdot \mathbf{U}_c \alpha (1 - \alpha) = 0, \quad (5)$$

Where  $\mathbf{U}_c$  is a velocity field suitable to compress the interface (Ma et al., 2018), and the last term at the left side is an anti-diffusion term utilized to sharpen the surface (Ma and Qian, 2018).

162

## 163 **2.2 Computational mesh for moving objects**

164 The numerical simulations are carried out on the platform of an open source  
165 package OpenFOAM. There are two different mesh systems used to deal with the flow  
166 problems with moving objects in OpenFOAM: deforming mesh and overset mesh, and  
167 both are adopted in the present study.

168 In deforming mesh, the grid points are attached to the surface of the wedge and  
169 move with the wedge. The mesh deformation region can be adjusted in the  
170 *dynamicMeshDict* tool in OpenFOAM. Parameter  $r$  represents the distance between  
171 the grid points and the wedge surface. With the definition of the inner-distance  $r_i$  and  
172 outer-distance  $r_o$  respectively, grid points at  $r < r_i$  move with the wedge to ensure  
173 that the finer cells around the wedge surface do not deform, whereas grid points at  
174  $r > r_o$  remain stationary. Therefore, only the grid points at  $r_i < r < r_o$  deform as the

wedge moves (Palm et al., 2016). Although deforming mesh is easy to implement, it cannot deal with the large amplitude motion very well. When the submerged part of the wedge is large, the quality of the grid becomes worse, possibly causing the simulation to diverge.

The overset mesh is composed of background mesh and sub-mesh, which exchanges flow information through the interpolation. As indicated in Fig. 2, the background mesh remains fixed in the computational domain, and sub-mesh is laid on top of the background mesh. The object is generated in the middle of the sub-mesh. Any background cell falling into the area occupied by the object is called the hole cell, which does not participate in the calculation of the flow field. Any cell connected with the hole cell is called the fringe cell. In Fig. 2, the red square cells on the background mesh and the green cells in the sub-mesh are the fringe cells. Fringe cells can be the receptors that receive flow information from the donors located in the adjacent grids. Sub-mesh moves in the background mesh, and the topology of the mesh remains unchanged. Because of the complex calculation in the overset mesh, the computation time using overset mesh is much longer than that for deforming mesh in the current version of OpenFOAM.

### **3. Validation**

A 2D numerical wave tank (NWT) is established with the abovementioned numerical methods in OpenFOAM. In order to validate the NWT model, the wedge

entry into the calm water is simulated and the numerical results are compared with the published data. The 2D numerical wave tank is  $3m$  long and  $2m$  height with a water depth of  $1m$ . The top side of the wedge has a length of  $1m$ . At the initial time, the wedge tip is placed on the free water surface, and then the wedge enters the water at a constant velocity  $v = 4m/s$ .

### 3.1 Deforming mesh analysis

In order to select the appropriate dynamic mesh, the deforming mesh is first adopted to simulate the water entry. In this case, the deadrise angle is set as  $45^\circ$ , and the mesh is generated by using the *snappyHexMesh* toolbox in OpenFOAM. As the wedge moves downwards, the mesh begins to deform as shown in Fig. 3. The calculation eventually diverges at  $t = 0.046s$ , due to the fact that the mesh is seriously distorted. The pressure coefficient  $C_p$  and free surface profile are shown in Fig. 4, which agree with the data in Zhao and Faltinsen (1993).  $C_p$  is defined as  $C_p = (p - p_0) / (0.5\rho v^2)$  where  $p_0 = 1bar$ ,  $v$  is the vertical velocity and  $p$  is the pressure on the wedge surface. It is suggested that the deforming mesh is only capable of dealing with bodies with small amplitude motions. Since the water entry problem considers a body with large amplitude motions, the overset mesh is used to carry out the simulations in the following study.

### 3.2 Mesh convergence study

In the present study, the overset mesh is generated by the *blockMesh*, a toolbox for

the generation of blocks of hexahedral cells in OpenFOAM. Fig. 5 presents the mesh topology of the NWT used in the simulation of wedge entry into the calm water. The background mesh covers the entire computational domain, and the sub-mesh occupies the area of  $1.6m$  long and  $0.8m$  height. In order to accurately capture the pressure, the mesh near the wedge surface is refined significantly. Because the computational area is relatively small and the object structure is simple, the mesh is evenly distributed with the uniform intervals of  $\Delta x$  and  $\Delta z$  in the horizontal and vertical directions respectively. To evaluate the sensitivity of the model regarding the mesh density, five different mesh schemes with different densities in the sub-mesh are adopted as shown in Table 1. In order to calculate the slamming force accurately, a rectangular region is mapped in the snappyHexMesh tool for partial refinement, and the refined factor is set to 2 for two mesh schemes in Table 1. The initial time step is set to 0.005, and the step size is changed dynamically at each time step according to the Courant number. The simulations are run on a workstation with Intel Xeon (R) E5-2699 v4 CPU, 128GB RAM, and a maximum number of 44 cores.

The pressure coefficient  $C_p$  for the five different mesh densities is presented in Fig. 6. Meanwhile, the comparison with the results in Zhao and Faltinsen (1993) indicates that the mesh resolution has little influence on the pressure coefficient except for the very coarse Mesh 5, but the finer mesh can certainly provide better results. It can be seen that the water jet is more sensitive to the mesh. While improving the mesh quality, the shape of the water jet becomes closer to the analytical solution. Results with both Mesh 1 and Mesh 2 are in good agreement with the published data, but the run

time of Mesh 1 is much more time-consuming compared to that of Mesh 2. After comprehensive consideration, Mesh 2 is chosen to carry out the following simulations.

### 3.3 Wedge entry into calm water

#### 3.3.1 Vertical entry

The vertical water entry of a symmetrical wedge with deadrise angles of  $45^\circ$  and  $60^\circ$  is simulated. For the sake of accuracy, the Courant number is set to 0.2. Fig. 7 shows the pressure coefficient distribution on the wedge surface and the water surface profile at  $t = 0.02s, 0.021s, 0.022s$ . Note that all the values here are dimensionless. It can be seen that the flow is self-similar, and the present numerical results are in good agreement with the similarity solution in Zhao and Faltinsen (1993). For the wedge with  $\gamma = 45^\circ$ , the pressure near the wedge tip is largest. In particular, a large pressure gradient can be observed near the root of the jet. At the top of the jet, the pressure is equal to the atmospheric pressure. For the wedge with  $\gamma = 60^\circ$ , the maximum pressure appears at the tip of the wedge and then rapidly decreases. It can be seen that at the start of the impact, water rises and jets along the surface of the wedge.

Furthermore, an asymmetric wedge with the left deadrise angle  $\gamma_1 = 50^\circ$  and the right deadrise angle  $\gamma_2 = 70^\circ$  is also studied. The simulation results are compared with the solutions produced by Xu et al. (2008), as shown in Fig. 8. The pressure distribution is asymmetric due to the different deadrise angles on two sides of the wedge. Since the left deadrise angle  $\gamma_1$  is greater than the right deadrise angle  $\gamma_2$ , the pressure on the left side of the wedge are greater than that on the right side. It is shown that the pressure

coefficient near the tip of the wedge is negative, which means that the pressure at the tip is lower than the atmospheric pressure because a certain amount of air can go with the wedge and be involved in the water when the wedge enters the water (Xu et al., 2008).

### 3.3.2 Oblique entry

The same symmetric wedge is adopted to study the oblique water entry. For this case, in addition to the same vertical entry velocity, the horizontal entry velocity  $u = 0.2\text{ m/s}, 0.6\text{ m/s}, 1\text{ m/s}$  is also considered. Fig. 9 shows the pressure distribution and the free surface profile for different horizontal entry velocities. It is clearly found that the present results coincide with the similarity solutions in (Xu et al., 2008). With the increase of the horizontal entry velocity, the pressure and the free surface on the right side also increase. It is found that with the larger horizontal entry velocity, the pressure near the left of the wedge tip is smaller than the similarity solution, which is due to the use of potential flow theory in the similarity solution.

Horizontal forces begin to appear when the deadrise angles on either side of the wedge are not equal, or during the oblique water entry. Horizontal forces  $f_x$  and vertical forces  $f_z$  on a symmetrical wedge in the oblique water entry are shown in Fig. 10. The  $f_x$  and  $f_z$  are normalized by  $\rho v^3 t$ , where  $t$  is the entry time. The results show that there is a linear relationship between the horizontal force and the velocity ratio. Vertical force is largely unaffected by the horizontal velocity (Xu et al., 2008). As the horizontal velocity  $u$  increases, the horizontal force gradually decreases and eventually becomes negative, whereas the vertical force also decreases but with a

milder slope. In the realistic offshore operation, when lifting the cargo into the water, the uneven force on the cargo surface should be avoided as far as possible. It is noted that the horizontal force on the asymmetric body could be offset in the oblique water entry.

## **4. Water entry of a wedge in waves**

Our study focuses on the investigation of water entry of payload hoisted by crane vessels under wave conditions. We have done some simulations of the influence of many parameters including the wedge geometric shape, the velocity of wedge entering into a wave, wave height, and entering a location into waves on hydrodynamic force and pressure distribution on wedges. During hoisting payloads entering into waves, the crane cable exerts force to payloads. It is ideal that the payloads enter into waves with a constant velocity. Therefore, a constant vertical velocity of the wedge is set in the simulation.

### **4.1 Configuration of 2D numerical wave tank**

In order to study wedge wave-entry, a numerical wave tank is set up first. The length and height of the wave tank are  $9.2m$  and  $2.1m$  respectively, and the water depth is  $1.5m$ . For the sake of safety, most crane vessels with crew work under up to the WMO sea state 2 (Chin et al., 2001) in practical applications. The World Meteorological Organization (WMO) defines the wave height under sea state 2 is from  $0.1m$  to  $0.5m$ , the wave height under sea state 1 is from  $0m$  to  $0.1m$ . The wave heights are set less than

0.5m in our simulation. The selection of wave parameters is also based on the previous literature (Sun et al., 2015; Cheng et al., 2018). The wave length and wave height are set as  $\lambda = 2.3m$  and  $H = 0.2m$  respectively. The wave period is  $T = 1.21s$ . The 5<sup>th</sup>-order Stokes wave is used in the present study. The configurations of the numerical wave tank and wedge are shown in Fig. 11, where the left boundary of the wave tank is the wave-maker, and the damping zone is on the right to avoid the wave reflection from the far-end boundary. IHFoam active wave absorption method (Higuera et al., 2014a; Higuera et al., 2014b) is used. Wave absorption is achieved by correcting the velocity value on the boundaries.

Near the inlet boundary of the tank and in the impact zone a relatively high mesh density is adopted, whereas a coarse mesh is distributed in the damping zone. Both the background mesh and sub-mesh in the impact zone have a grid size of 0.01m in the two directions. The wave parameters such as wave type, wave height and wave period are set in the *waveProperties* tool in OpenFOAM. At the beginning of the water entry at  $t = 0s$  the tip of the wedge is at the peak of the wave and the wedge starts to enter the wave at a constant vertical entry velocity. It should be noted that the body frame ( $xOz$ ) moves with the wedge.

In order to ensure the wedge to enter the wave at the right location (wave peak, wave trough, or cross point with the still water level), the *motionSolver* is modified in OpenFOAM. Since the rigid body is attached to the sub-mesh point and moves with the sub-mesh, a function is compiled in the *motionSolver* to preset the motion of the sub-mesh, which updates the motion of the rigid body by updating the mesh displacement.



Several wave cycles are initially generated before the wedge entering into the waves. According to identify the free surface of the wave, the location of the wedge in the air is adjusted which ensures the wedge reaches the desired entry location (wave peak, wave trough, and cross point with the still water level) at beginning of water entry. After touching the free surface, the wedge is driven into the water by the *motionSolver* with a constant velocity.

## **4.2 Symmetry wedge entry into waves**

### **4.2.1 Influence of wave height**

In practical engineering applications, sea condition is a key factor for the safe hoisting operation of crane vessels. Total force and pressure distribution on wedges are analyzed with different wave heights in the simulation. In this section, the symmetric wedge with  $45^\circ$  deadrise angles is considered. Three different wave heights  $H=0.05m$ ,  $0.1m$ ,  $0.2m$  are considered in this study to evaluate its influence on the pressure distribution and total force, which are shown in Fig. 12 and Fig. 13. The difference of the pressure between two sides of the wedge increases with the increase of wave height. When the entry time  $t$  is small, a small part of the wedge is submerged in the wave and the local wave is nearly undisturbed. Therefore, the factor that affects the pressure distribution is the horizontal wave velocity. Larger wave height can lead to faster horizontal velocity, causing a more pronounced difference of wedge pressure distribution between two sides (Sun et al., 2015). As a more part of the wedge is submerged in the wave, the deadrise angle becomes the main factor to influence the

pressure distribution. Previous literature (Zhao and Faltinsen, 1993) and our study in subsection 3.3 have shown that a smaller deadrise angle leads to greater pressure. In the case of wedge entering waves, the effective deadrise angle depends on the angle between the wedge surface and the sloping wave surface. As the wave height decreases, the effective deadrise angles on both sides of the wedge become smaller, which leads to larger pressure.

Time series of horizontal force  $F_x$  and vertical force  $F_z$  on the wedge are shown in Fig. 13. In the case of peak entry, the vertical force on the wedge increases with time, because of the increasing wetted wedge surface. As the wedge continues moving down, the vertical force gradually decreases until the hydrostatic pressure begins to take effect. From the entry time  $t=0.1s$ , the hydrostatic pressure starts to increase with the depth of the wedge, causing the upward vertical force to rise eventually. Smaller wave height results in greater pressure, as shown in Fig. 13, so the vertical force decreases as the wave height increases.

The change of horizontal force is more complicated. At the initial stage of the water entry, both sides of the wedge have the same relative deadrise angle. Due to the horizontal velocity of the wave peak, the pressure on the left side is higher. As the entry time  $t$  increases and the wave moves, the right side of the wedge submerges in the wave faster; therefore, the right side has the larger contact area with the wave. It leads the hydrodynamic force on the right side to grow faster, and the horizontal force pointing to the right to decrease. When the right side of the wedge is completely submerged in the water, the horizontal force increases again. Due to the fact that both sides of the

wedge are fully submerged and the effect of the horizontal velocity disappears, the horizontal force decreases and becomes zero eventually.

#### **4.2.2 Influence of entry velocity**

In the practical hoisting operation of crane vessels, vertical entry velocity can affect safety and efficiency. We study the influence of the vertical entry velocity on the total force and pressure distribution of the wedge. Three different entry velocities  $v=2m/s$ ,  $3.16m/s$ ,  $6m/s$  are considered to investigate the influence on the water entry of a wedge in waves. Since the wave velocity and relative deadrise angle are varying at different entry distance to the free water surface, we compare the results at the same entry distance. Fig. 14 shows the pressure distribution for different entry velocities. With the increase of velocity, the pressure coefficient difference between the left and right sides decreases. When a large part of the wedge is submerged in the wave, the relative deadrise angle determines the pressure distribution. Therefore, the final pressure distribution at three speeds tends to be the same.

The total forces are shown in Fig. 15, from which we can see that larger velocity causes a larger vertical force and an earlier peak of the vertical force. The entry velocity has a great influence on the hydrodynamic force amplitude. In addition, the vertical force decreases more after the peak with the larger velocity. It can be seen that the vertical force with the water entry velocity of  $2m/s$  is very steady without any fluctuation after the force peak. The variation trend of the horizontal force on the wedge with three water entry velocities is almost the same as that of the vertical force in that faster entry speed can give an earlier peak but larger horizontal force.

### 4.2.3 Influence of entry location

In the practical hoisting operation of crane vessels, entry location in waves can affect the total force on payloads. In the present study, three typical locations where the water entry occurs are selected, which are the wave peak, the cross point with the still water level, and the wave trough. It can be found in Fig. 16 that the pressure on the left side of the wedge is relatively higher when the wedge enters the wave peak, while it is opposite at the wave trough. This is because for the symmetric wedge the pressure distribution is mainly determined by the horizontal wave velocity. At the wave peak, the horizontal wave velocity is to the right but opposite at the trough. As the wedge moves into the wave, because the relative deadrise angle at the wave trough is smaller, the pressure at the trough is greater than the pressure at the peak. In case of the entry at the cross point, the wave slope causes a smaller deadrise angle on the left of the wedge, so the pressure is greater on the left side of the wedge. Similarly, since the relative deadrise angle is smallest, the pressure at the cross point entry is larger than those of the wave entry at the other two locations. At  $t=0.04s$ , it should be noted that the left side of the wedge at the cross point entry is completely submerged, so the pressure on the left side begins to decrease.

The total forces on the wedge with different entry locations are compared in Fig. 17. When the wedge enters the water at the cross point, the left side of the wedge submerges in the water more quickly. Vertical force reaches the peak when all the left side is completely submerged in the water, while the right side is still in the jet. The reasons for this phenomenon are as follows: firstly, the relative deadrise angle of the

left side is small, and the total force on the left side accounts for the main part of the total force. Secondly, the pressure on the left side decreases sharply, after the left side has completely submerged in the water. Vertical force at the trough entry is similar to that at the peak entry. Because the relative deadrise angle at the trough entry is smaller, the vertical force is larger than that at the peak entry.

In the case of the cross point entry, peak of the horizontal force occurs when all the left side of the wedge is submerged. Also because of the deadrise angle, the horizontal force at the cross point entry is much larger than the other two cases. It should be noted that the horizontal force at the trough entry is opposite to that at the crest entry, due to the difference in the horizontal velocity between the two conditions.

### **4.3 Asymmetry wedge entry into waves**

In realistic engineering practice, plenty of asymmetric payloads need to be hoisted into the wave. For example, in the construction of the submarine platform, the bottom of many components that need to be installed underwater is asymmetric. To provide helpful information for the selection of water entry velocity and location of the payload, the pressure distribution on the asymmetric wedge with the deadrise angles of  $\gamma_1 = 30^\circ$  and  $\gamma_2 = 60^\circ$  entering waves are studied. The deadrise angles on both sides are also swapped to consider the influence of the reversed asymmetry. Other than the change of the wedge geometry to the asymmetric one, all the other computational conditions are the same as the symmetric situations.

### 4.3.1 Influence of wave height for asymmetric wedge

Fig. 18 shows the pressure distribution on the asymmetric wedge entering waves. With the left deadrise angle of the wedge decreasing, the pressure there increases. At  $t=0.05s$ , the horizontal velocity of the wave affects the pressure distribution, resulting in a strong negative pressure near the wedge tip. As a greater part of the wedge is submerged in waves, the pressure on the wedge surface gradually decreases. It can be seen that the higher the wave height, the faster the horizontal velocity and the higher the initial pressure on the left side of the wedge. As the entry time  $t$  increases, because the effective deadrise angle increases, the pressure on the wedge surface decreases with the increase of the wave height  $H$ . The pressure distribution on the reversed asymmetric wedge is shown in Fig. 19. It is known in the last section that the horizontal velocity has an effect on the pressure on the left side of the symmetric wedge. However, for the asymmetric wedge, the influence of horizontal velocity on the pressure coefficient becomes less obvious.

Fig. 20 shows the free surface profile for the entry of the asymmetric wedge at different time instants. The jet on the side with a smaller deadrise angle becomes longer, but it is reduced on the other side because the smaller deadrise angle has a larger contact area. After the jet detaches from the wedge surface, the jet begins to bend downward because of the influence of gravity. Fig. 21 shows the jet velocity around the wedges at  $t = 0.3s$ , and the red color represents the faster speed. The jet on the side with a smaller deadrise angle is faster compared to the other side. Due to the horizontal velocity of the incident waves, the jet velocity in Fig. 21(b) is larger than that in Fig. 21(a).

Furthermore, the fluid horizontal velocity has a sharp variation near the wedge vertex, which results in a sudden drop of the pressure near the wedge vertex (Cheng et al., 2018).

In the water entry of the asymmetric wedge, the side with the small deadrise angle plays a major role in the hydrodynamic force. The smaller deadrise angle leads to a larger pressure and a larger force area, which greatly increases the total forces on the wedge. Therefore, for the water entry of asymmetrical wedges, all the total force peaks occur when the side with the smaller deadrise angle is submerged in the wave completely.

Fig. 22 presents the total forces with the deadrise angles  $\gamma_1 = 30^\circ$  and  $\gamma_2 = 60^\circ$  at different incident wave heights. The peak of the vertical force occurs when the wedge is completely submerged in the wave. After the left side of the wedge enters the water completely, the pressure on the left side decreases rapidly and the horizontal force drops. Then, the vertical force rises again because of the influence of the hydrostatic pressure. The vertical force on the reversed asymmetry wedge in Fig. 23 changes the same as on the wedge described above. However, since the right side of the wedge submerges in the wave faster at the crest entry, the inverted wedge reaches the peak earlier and the horizontal force peak is larger than the previous asymmetric wedge. The horizontal force peaks on both asymmetrical wedges occur when the side with the small deadrise angle is completely submerged.

#### **4.3.2 Influence of entry velocity for asymmetric wedge**

Fig. 24 and Fig. 25 show the pressure distribution obtained for different entry

483 velocities. The horizontal velocity of a wave has a greater effect on the side with a  
484 smaller deadrise angle of the wedge. Compared to the asymmetrical wedge pressure  
485 distribution in Fig. 24, the horizontal velocity has less influence on the pressure  
486 distribution on the reversed asymmetric wedge, and the pressure distribution with  
487 different entry velocities is basically the same.

488 The total forces on asymmetric wedges are shown in Fig. 26 and Fig. 27. The effect  
489 of velocity on total forces is obvious. The change in horizontal forces is similar to the  
490 symmetric wedge case, where the faster speed causes a greater total force. Compared  
491 with the symmetric wedge case, the horizontal force on the asymmetric wedge is more  
492 sensitive to the entry velocity. It is interesting to see that with the increase of entry  
493 velocity, the change in the horizontal force on the asymmetric wedge is much larger  
494 than the change in the symmetric wedge case.

#### 495 **4.3.3 Influence of entry location for asymmetric wedge**

496 Fig. 28 shows the pressure distribution on the first asymmetric wedge at different  
497 water entry locations. When the wedge enters the wave at the cross point, the peak of  
498 pressure coefficient occurs far away from the wedge tip, and the pressure coefficient is  
499 much larger than that at the peak and trough entries. At  $t = 0.04s$  the pressure coefficient  
500 on the left side of the asymmetrical wedge with the deadrise angles  $\gamma_1 = 30^\circ$  and  
501  $\gamma_2 = 60^\circ$  decreases sharply in the case of cross point entry and trough entry. The reason  
502 is that the wedge considered in this paper is of finite volume and the left side of the  
503 wedge is completely submerged in the wave at  $t = 0.04s$ . For the reversed asymmetric  
504 wedge in Fig. 29, the pressure peak is largest at the trough entry because the slope of



the wave reduces the relative deadrise angle on the right side of the wedge. It is worth noting that the pressure coefficient on both sides of the wedge is relatively balanced at the cross point entry.

In Fig. 30, the deadrise angle of the wedge is smaller at the incoming wave side, so the vertical force at the cross point entry reaches the peak faster. In the case of the reversed asymmetric wedge, the small deadrise angle is at the lee side, which reduces the vertical force on the wedge. As can be seen from Fig. 31, on the asymmetric wedge with the deadrise angles  $\gamma_1 = 60^\circ, \gamma_2 = 30^\circ$ , the horizontal force at the cross point entry has a significant turning point before the peak. The reason is that the left side of the wedge submerges faster, which causes the horizontal force on the left side of the wedge to increase rapidly and the resultant horizontal force increases slowly. After the left side of the wedge is completely submerged in the water and the force area on the left side remains unchanged, the force to the left increases faster.

## 5. Conclusion

In order to provide helpful guidance to the design of the control system of the ship crane during offshore operations, an overset mesh based numerical wave tank is presented to simulate water entry problems of a symmetric/asymmetric wedge into waves. By using this numerical wave tank, a 2D wedge entry into the calm water is first simulated. The present results agree well with the data in the literature, which shows the accuracy of the present numerical model for the water entry problem.

For the water entry of a wedge into waves, total force characteristics of water entry process until the wedge is fully submerged are investigated. The numerical results suggest that the side with the small deadrise angle plays an important role in affecting the hydrodynamic characteristics. It ought to be noted that the vertical and horizontal forces become larger with the faster entry velocity, although the dimensionless pressure coefficient appears to be more balanced on both sides. For the symmetric wedge, the force on both sides is more balanced when the wedge enters the water at the wave peak or wave trough locations. For the asymmetric wedge, the deadrise angle difference between the two sides can be reduced when entering the water at the cross point location, and the effect of horizontal velocity of the wave on the wedge is almost negligible when the side with the smaller deadrise angle faces the incoming wave.

## Acknowledgments

This work is supported by the Joint Funds of the National Natural Science Foundation of China-Shandong Province (Grant No. U1706228).

## Reference :

- Barjasteh, M., Zeraatgar, H., Javaherian, M.J., 2016. An experimental study on water entry of asymmetric wedges. *Appl. Ocean Res.* 58, 292-304. <https://doi.org/10.1016/j.apor.2016.04.013>.
- Chan, W.M., 2009. Overset grid technology development at NASA Ames Research Center. *Comput. Fluids* 38 (3), 496-503. <https://doi.org/10.1016/j.compfluid.2008.06.009>.
- Chandar, D.D., Boppana, B., Kumar, V., 2018. A comparative study of different overset grid solvers between OpenFOAM, StarCCM+ and ansys-fluent. In: *AIAA Aerospace Sciences Meeting*. American Institute of Aeronautics and Astronautics, Reston, Virginia, pp. 22 2018.

554 Chen, H., Qian, L., Ma, Z., Bai, W., Li, Y., Causon, D., Mingham, C., 2019. Application  
 555 of an overset mesh based numerical wave tank for modelling realistic free-surface  
 556 hydrodynamic problems. *Ocean Eng.* 176, 97-117.  
 557 <https://doi.org/10.1016/j.oceaneng.2019.02.001>.  
 558 Cheng, Y., Ji, C., Zhai, G., Oleg, G., 2018. Numerical investigation of water entry of a  
 559 wedge into waves with current effects using a fully nonlinear HOBEM. *Ocean Eng.*  
 560 153, 33-52. <https://doi.org/10.1016/j.oceaneng.2018.01.092>.  
 561 Chin, C.-M., Nayfeh, A.H., Mook, D.T., 2001. Dynamics and Control of Ship-Mounted  
 562 Cranes. *J. Vib. Control* 7 (6), 891-904.  
 563 Dobrovol'skaya, Z.N., 1969. On some problems of similarity flow of fluid with a free  
 564 surface. *J. Fluid Mech.* 36 (4), 805-829. <https://doi.org/10.1017/S0022112069001996>.  
 565 Driscoll, F., Lueck, R., Nahon, M., 2000. The motion of a deep-sea remotely operated  
 566 vehicle system: Part 1: motion observations. *Ocean Eng.* 27 (1), 29-56.  
 567 [https://doi.org/10.1016/s0029-8018\(98\)00076-6](https://doi.org/10.1016/s0029-8018(98)00076-6).  
 568 Gu, H.B., Qian, L., Causon, D.M., Mingham, C.G., Lin, P., 2014. Numerical simulation  
 569 of water impact of solid bodies with vertical and oblique entries. *Ocean Eng.* 75, 128-  
 570 137. <https://doi.org/10.1016/j.oceaneng.2013.11.021>.  
 571 Higuera, P., Lara, J.L., Losada, I.J., 2014a. Three-dimensional interaction of waves and  
 572 porous coastal structures using OpenFOAM. Part I: formulation and validation. *Coastal*  
 573 *Eng.* 83, 243-258.  
 574 Higuera, P., Lara, J.L., Losada, I.J., 2014b. Three-dimensional interaction of waves and  
 575 porous coastal structures using OpenFOAM. Part II. application. *Coastal Eng.* 83, 259-  
 576 270.  
 577 Hirt, C.W., Nichols, B.D., 1981. Volume of fluid (VOF) method for the dynamics of  
 578 free boundaries. *J. Comput. Phys.* 39 (1), 201-225. [https://doi.org/10.1016/0021-9991\(81\)90145-5](https://doi.org/10.1016/0021-9991(81)90145-5).  
 579 [https://doi.org/10.1016/0021-9991\(81\)90145-5](https://doi.org/10.1016/0021-9991(81)90145-5).  
 580 Hover, F.S., Grosenbaugh, M.A., Triantafyllou, M.S., 1994. Calculation of dynamic  
 581 motions and tensions in towed underwater cables. *IEEE J. Oceanic Eng.* 19 (3), 449-  
 582 457. <https://doi.org/10.1109/48.312921>.  
 583 Hu, Z., Zhao, X., Li, M., Fang, Z., Sun, Z., 2018. A numerical study of water entry of  
 584 asymmetric wedges using a CIP-based model. *Ocean Eng.* 148, 1-16.  
 585 <https://doi.org/10.1016/j.oceaneng.2017.11.011>.  
 586 Kleefsman, K.M.T., Fekken, G., Veldman, A.E.P., Iwanowski, B., Buchner, B., 2005. A  
 587 Volume-of-Fluid based simulation method for wave impact problems. *J. Comput. Phys.*  
 588 206 (1), 363-393. <https://doi.org/10.12989/ose.2018.8.2.183>.  
 589 Ma, Z., Qian, L., 2018. Numerical simulation of wave slamming on wedges and ship  
 590 sections during water entry. *Ocean Systems Engineering* 8 (2), 183-199.  
 591 <https://doi.org/doi.org/10.12989/ose.2018.8.2.183>.  
 592 Ma, Z.H., Qian, L., Martínez-Ferrer, P.J., Causon, D.M., Mingham, C.G., Bai, W., 2018.  
 593 An overset mesh based multiphase flow solver for water entry problems. *Comput.*  
 594 *Fluids* 172 (0), 689-705. <https://doi.org/10.1016/j.compfluid.2018.01.025>.  
 595 Oger, G., Doring, M., Alessandrini, B., Ferrant, P., 2006. Two-dimensional SPH  
 596 simulations of wedge water entries. *J. Comput. Phys.* 213 (2), 803-822.  
 597 <https://doi.org/10.1016/j.jcp.2005.09.004>.

Palm, J., Eskilsson, C., Paredes, G.M., Bergdahl, L., 2016. Coupled mooring analysis for floating wave energy converters using CFD: Formulation and validation. *Int. J. Mar. Energy* 16, 83-99. <https://doi.org/10.1016/j.ijome.2016.05.003>.

Panciroli, R., Abrate, S., Minak, G., Zucchelli, A., 2012. Hydroelasticity in water-entry problems: Comparison between experimental and SPH results. *Compos. Struct.* 94 (2), 532-539. <https://doi.org/10.1016/j.compstruct.2011.08.016>.

Semenov, Y.A., Iafrati, A., 2006. On the nonlinear water entry problem of asymmetric wedges. *J. Fluid Mech.* 547, 231-256. <https://doi.org/10.1017/s0022112005007329>.

Shen, Z., Wan, D., Carrica, P.M., 2015. Dynamic overset grids in OpenFOAM with application to KCS self-propulsion and maneuvering. *Ocean Eng.* 108, 287-306. <https://doi.org/10.1016/j.oceaneng.2015.07.035>.

Sun, S.Y., Sun, S.L., Wu, G.X., 2015. Oblique water entry of a wedge into waves with gravity effect. *J. Fluids Struct.* 52, 49-64. <https://doi.org/10.1016/j.jfluidstructs.2014.09.011>.

Tassin, A., Piro, D.J., Korobkin, A.A., Maki, K.J., Cooker, M.J., 2013. Two-dimensional water entry and exit of a body whose shape varies in time. *J. Fluids Struct.* 40, 317-336. <https://doi.org/10.1016/j.jfluidstructs.2013.05.002>.

Wang, J., Zou, L., Wan, D., 2017. CFD simulations of free running ship under course keeping control. *Ocean Eng.* 141, 450-464. <https://doi.org/10.1016/j.oceaneng.2017.06.052>.

Wen, P., Qiu, W., 2015. Solving 2-D water entry problems with a CIP method and a parallel computing algorithm. *Marine Systems & Ocean Technology* 11, 1-9. <https://doi.org/10.1007/s40868-015-0012-5>.

Wu, G.X., Sun, H., He, Y.S., 2004. Numerical simulation and experimental study of water entry of a wedge in free fall motion. *J. Fluids Struct.* 19 (3), 277-289. <https://doi.org/10.1016/j.jfluidstructs.2004.01.001>.

Xu, G.D., Duan, W.Y., Wu, G.X., 2008. Numerical simulation of oblique water entry of an asymmetrical wedge. *Ocean Eng.* 35 (16), 1597-1603. <https://doi.org/10.1016/j.oceaneng.2008.08.002>.

Yang, Q., Qiu, W., 2012. Numerical simulation of water impact for 2D and 3D bodies. *Ocean Eng.* 43, 82-89. <https://doi.org/10.1016/j.oceaneng.2012.01.008>.

Zhao, R., Faltinsen, O.M., 1993. Water entry of two-dimensional bodies. *J. Fluid Mech.* 246 (1), 593-612. <https://doi.org/10.1017/s002211209300028x>.

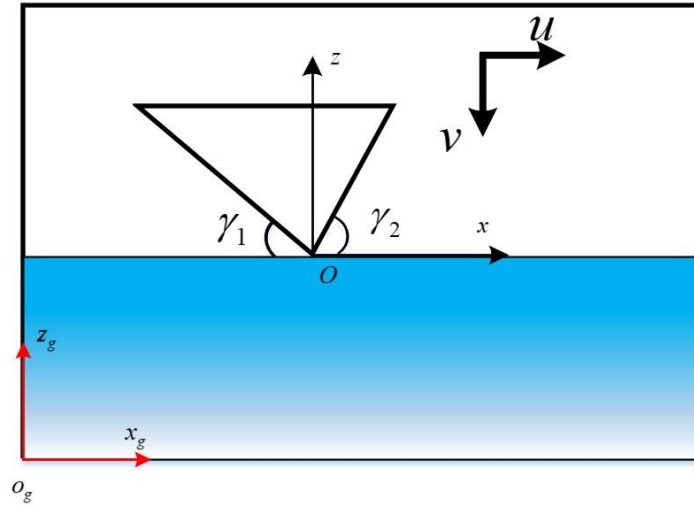


Fig. 1 An overview of the 2D water entry problem

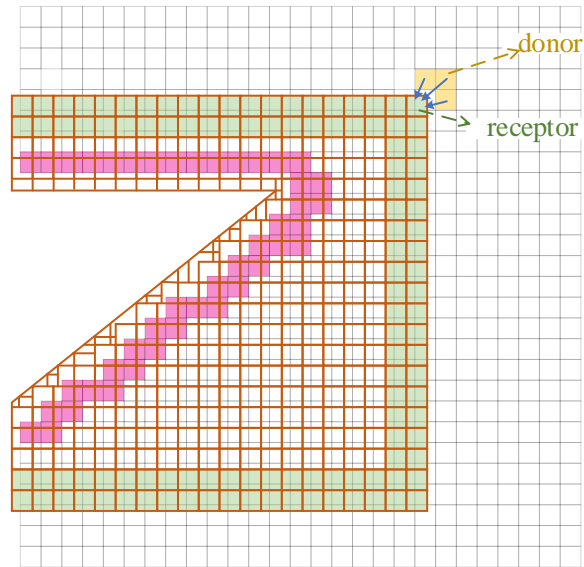


Fig. 2 Sketch of overset and background mesh. The green cells are the front fringe cells in the overset mesh, the red cells are the back-fringe cells in the background mesh, and the yellow cells are the donors.

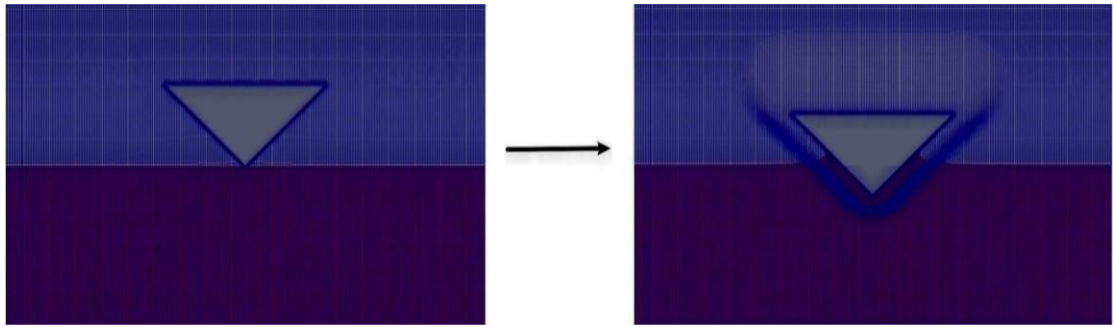


Fig. 3 Mesh deformation in water entry simulations. Left: Initial mesh. Right:

Deforming mesh with the wedge motion.

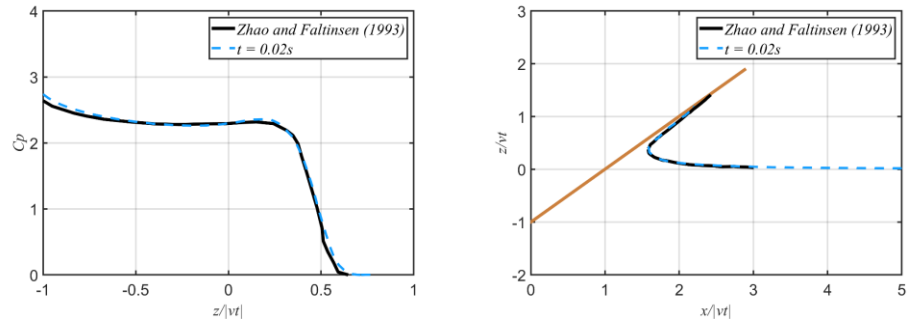
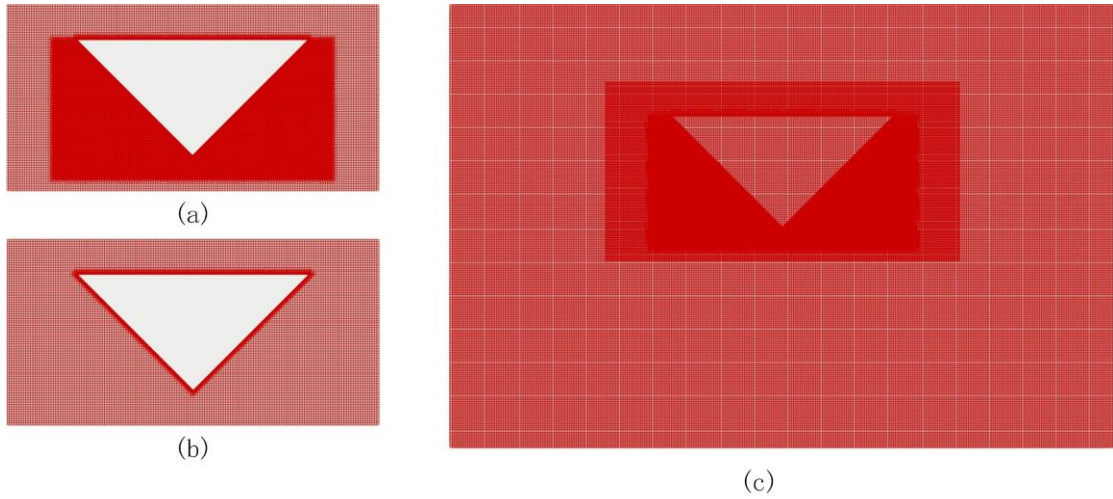


Fig. 4 Numerical results obtained by the deforming mesh. Left: Pressure coefficient on the wedge surface. Right: Free surface profile.





648

649 Fig. 5 Mesh around the symmetric wedge. Left: (a) Refined sub-mesh; (b) Unrefined

650

sub-mesh; (c) An overview of the mesh.

651

652

Table 1 Mesh parameters and computation cost.

Mesh scheme	$\Delta x = \Delta z$	Refinement factor	Run time
1	0.005 <i>m</i>	-	43.9 <i>h</i>
2	0.01 <i>m</i>	2	8.5 <i>h</i>
3	0.01 <i>m</i>	-	1.97 <i>h</i>
4	0.02 <i>m</i>	2	0.5 <i>h</i>
5	0.02 <i>m</i>	-	0.3 <i>h</i>

653

654

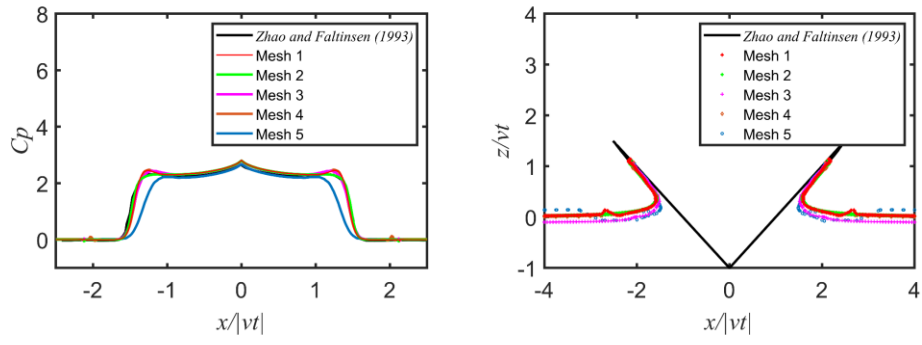
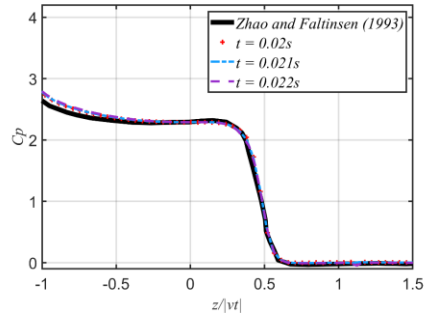
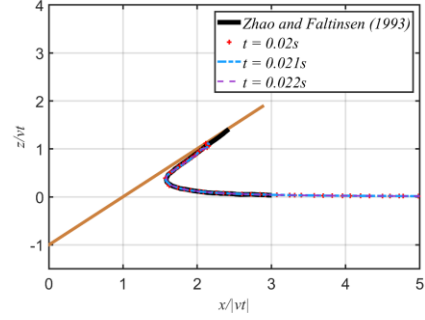


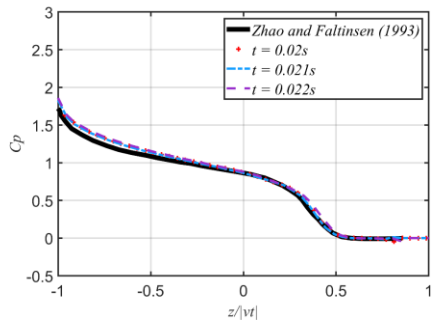
Fig. 6 Pressure distribution (left) and free surface profile (right) for the water entry of the wedge using five mesh schemes.



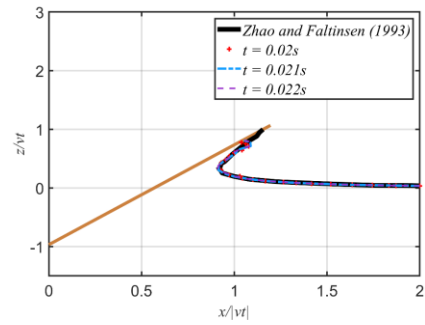
(a) Pressure coefficient for  $\gamma = 45^\circ$



(b) Surface profile for  $\gamma = 45^\circ$



(c) Pressure coefficient for  $\gamma = 60^\circ$



(d) Surface profile for  $\gamma = 60^\circ$

Fig. 7 Pressure coefficient distribution and free surface profile on the symmetric wedge surface.

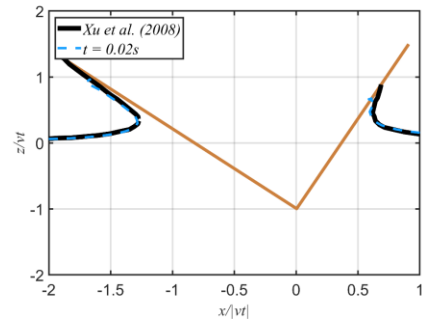
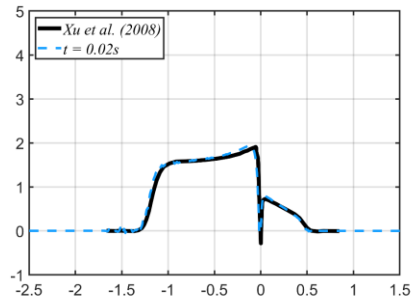


Fig. 8 Pressure coefficient and free surface profile on the asymmetric wedge.

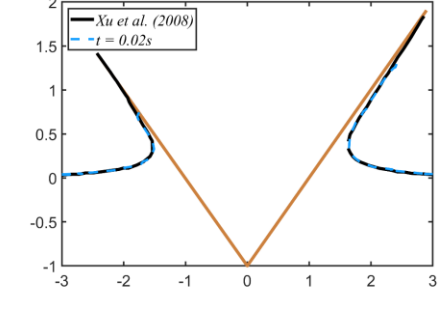
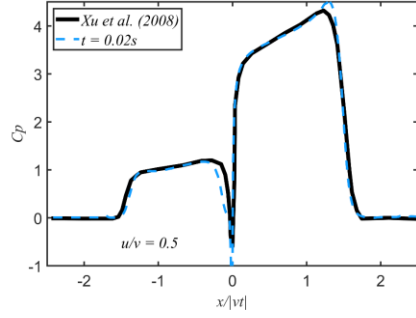
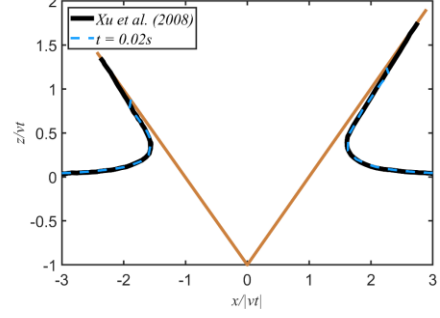
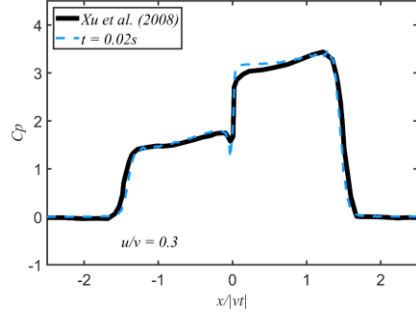
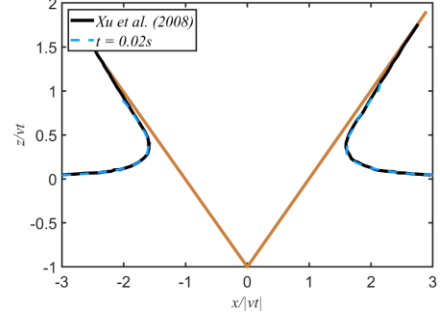
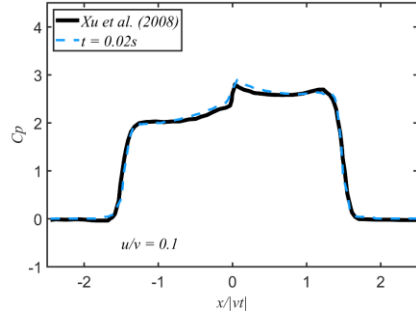
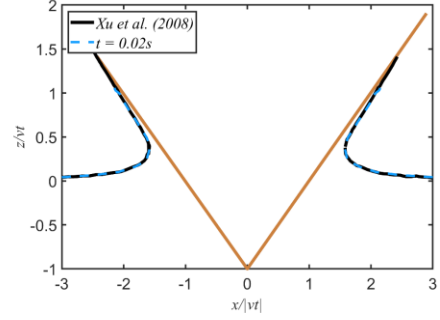
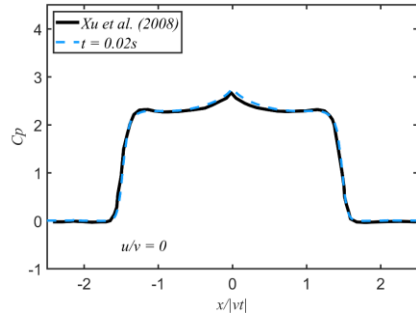


Fig. 9 Oblique water entry of a symmetric wedge. Left: Pressure coefficient distribution; Right: Free surface profile.

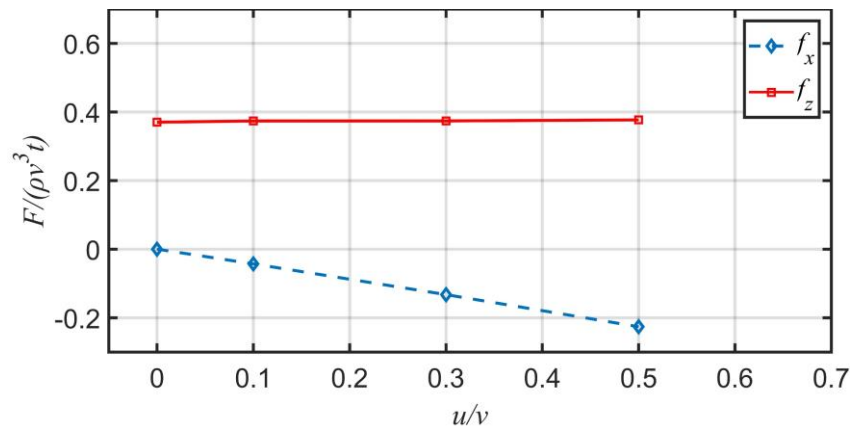


Fig. 10 Vertical and horizontal forces on the wedge.

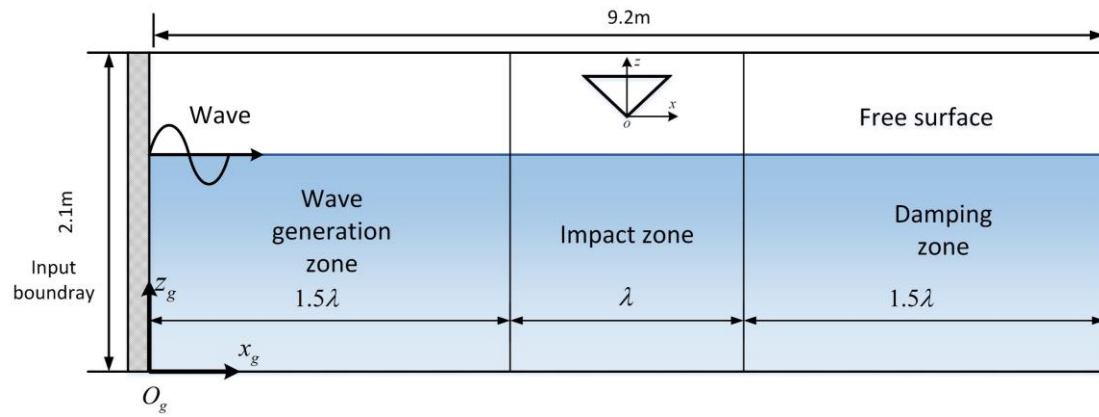


Fig. 11. Sketch of the 2D numerical wave tank for water entry of a wedge into waves.



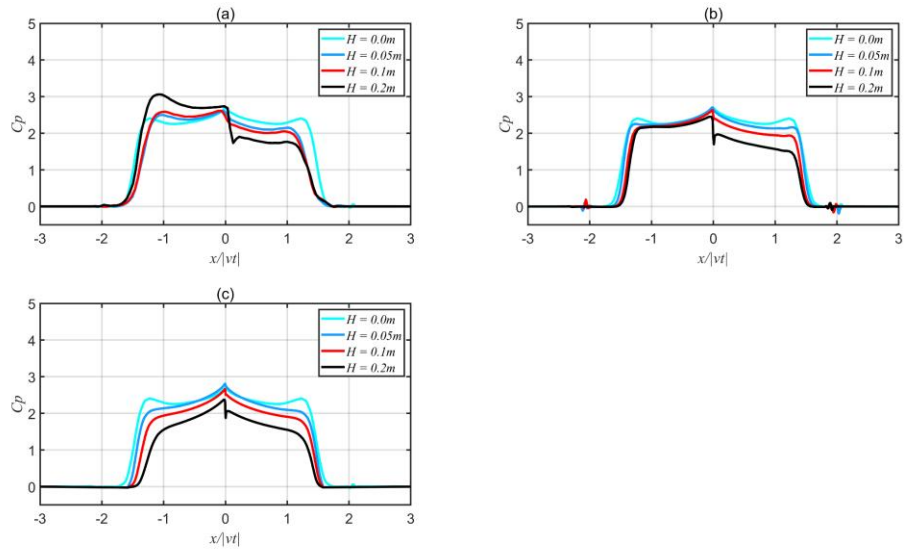


Fig. 12. Pressure distribution for wave entry of a symmetric wedge with different wave heights. (a)  $t = 0.004s$ , (b)  $t = 0.02s$ , (c)  $t = 0.04s$ .

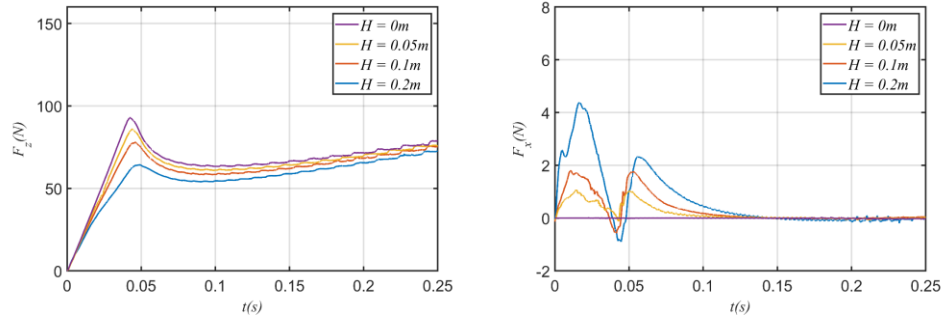
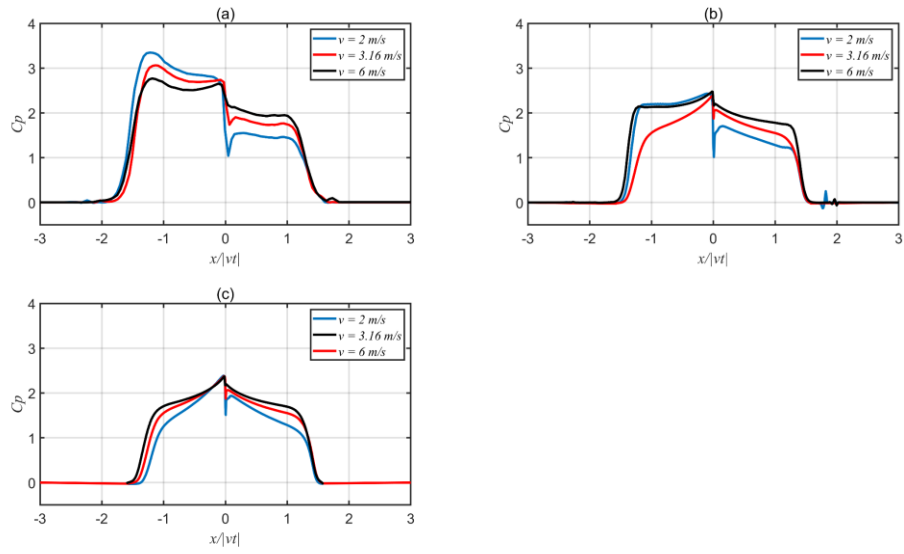


Fig. 13 Total force for wave entry of a symmetric wedge with different wave heights.

689



690

691 Fig. 14. Pressure distribution for wave entry of a symmetric wedge with different  
 692 velocities. (a)  $s = 0.004 \cdot 3.16 \text{ m}$ , (b)  $s = 0.02 \cdot 3.16 \text{ m}$ , (c)  $s = 0.04 \cdot 3.16 \text{ m}$ . Here  $s$  is the  
 693 entry distance to the free water surface.

694

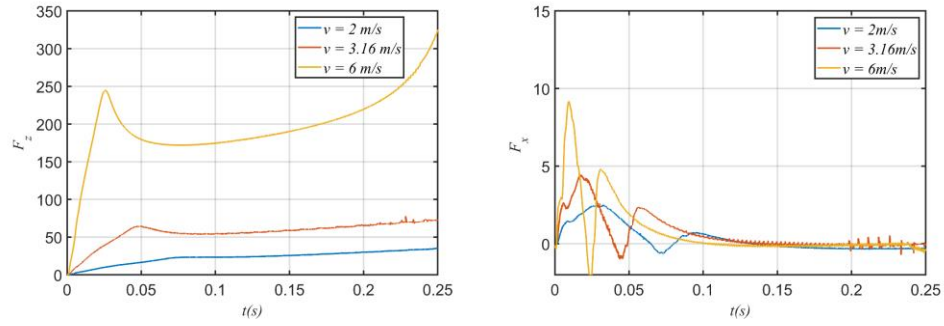


Fig. 15 Total force for wave entry of a symmetric wedge with different velocities.

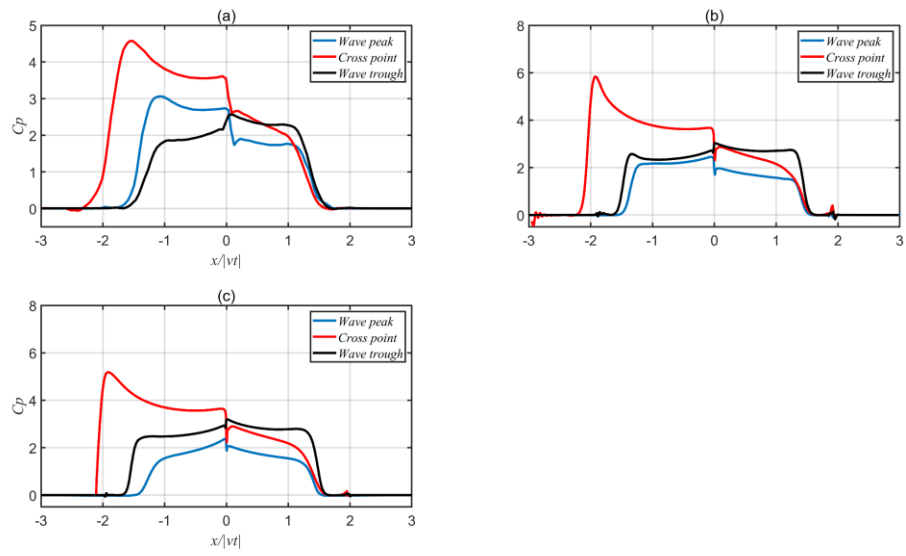


Fig. 16 Pressure distribution for wave entry of a symmetric wedge with different entry locations. (a)  $t = 0.004s$ , (b)  $t = 0.02s$ , (c)  $t = 0.04s$ .

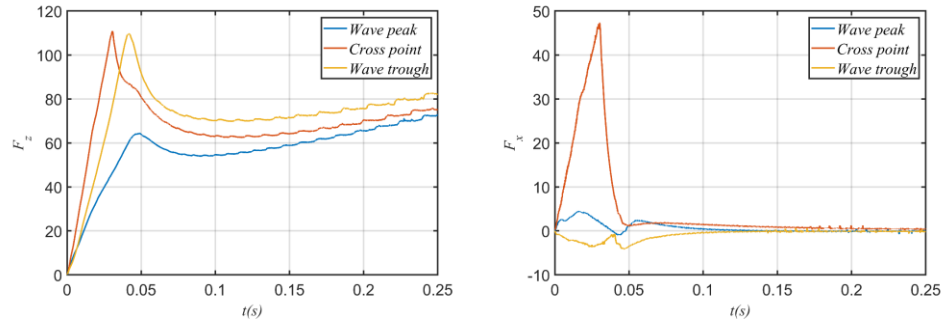


Fig. 17. Total force for wave entry of a symmetric wedge with different entry

locations.

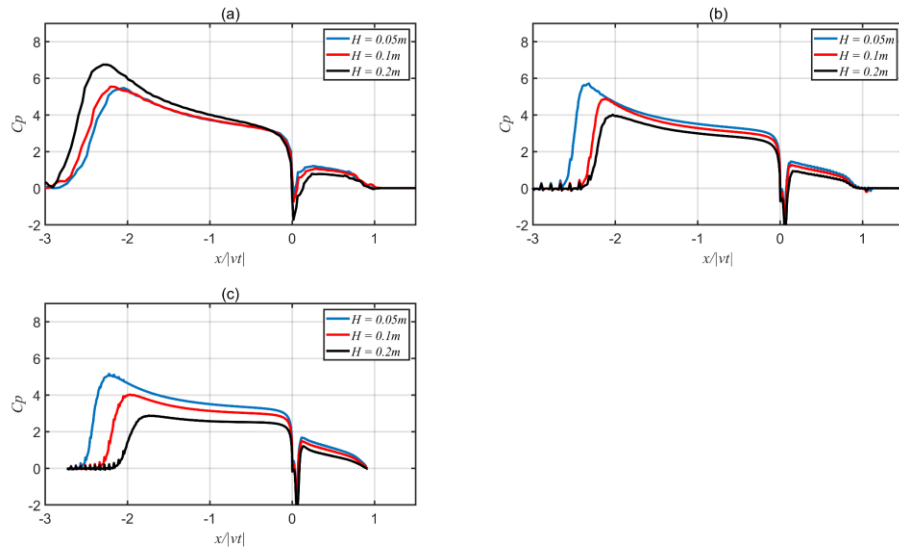


Fig. 18. Pressure distribution for wave entry of an asymmetric wedge of  $\gamma_1 = 30^\circ$ ,  $\gamma_2 = 60^\circ$  with different wave heights. (a)  $t = 0.004s$ , (b)  $t = 0.02s$ , (c)  $t = 0.04s$ .

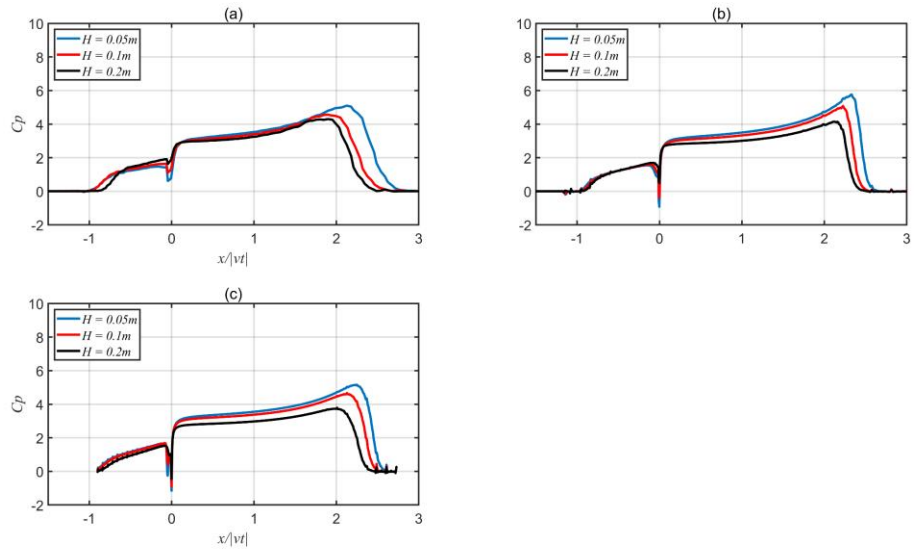


Fig. 19. Pressure distribution for wave entry of an asymmetric wedge of  $\gamma_1 = 60^\circ$ ,  $\gamma_2 = 30^\circ$  with different wave heights. (a)  $t = 0.004s$ , (b)  $t = 0.02s$ , (c)  $t = 0.04s$ .



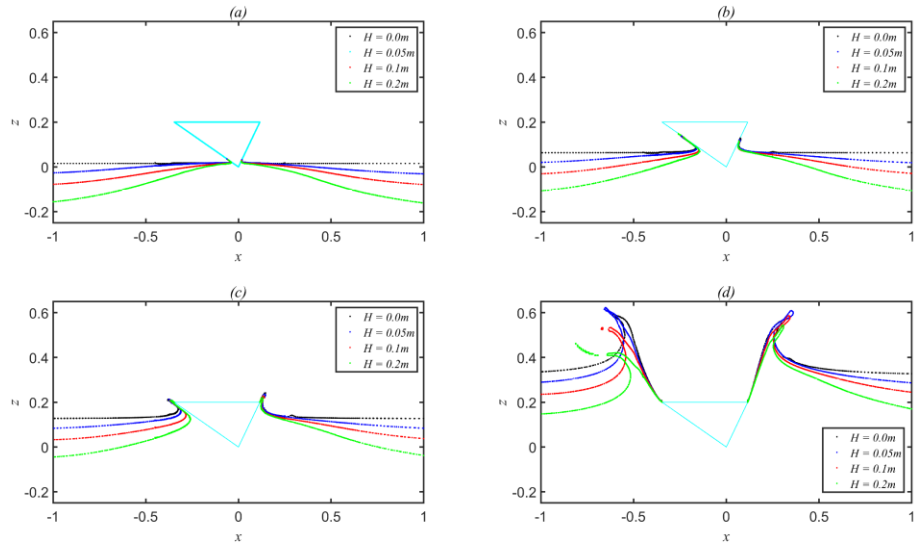


Fig. 20 Free surface profile for wave entry of an asymmetric wedge of  $\gamma_1 = 30^\circ$ ,  $\gamma_2 = 60^\circ$  with different wave heights. (a)  $t = 0.004s$ , (b)  $t = 0.02s$ , (c)  $t = 0.04s$ , (d)  $t = 0.1s$ .

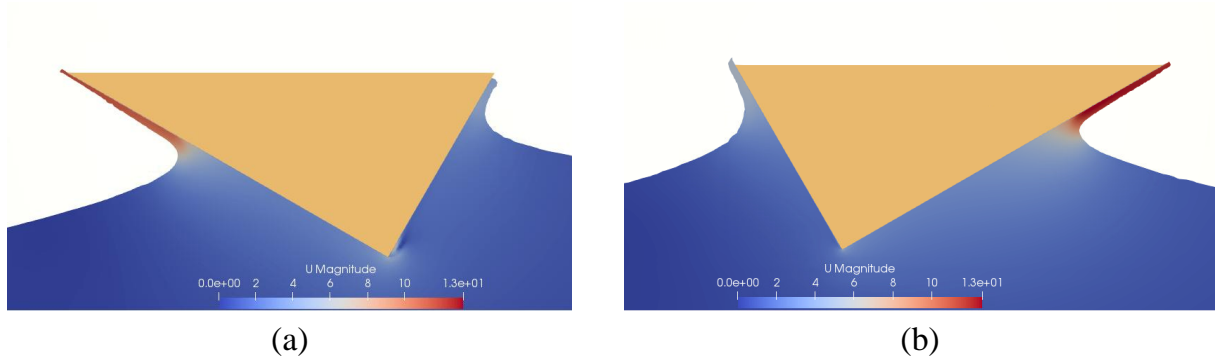


Fig. 21 Jet velocity of asymmetric wedges at  $t = 0.03s$ . (a) An asymmetric wedge of  $\gamma_1 = 30^\circ, \gamma_2 = 60^\circ$ . (b) An asymmetric wedge of  $\gamma_1 = 60^\circ, \gamma_2 = 30^\circ$ .

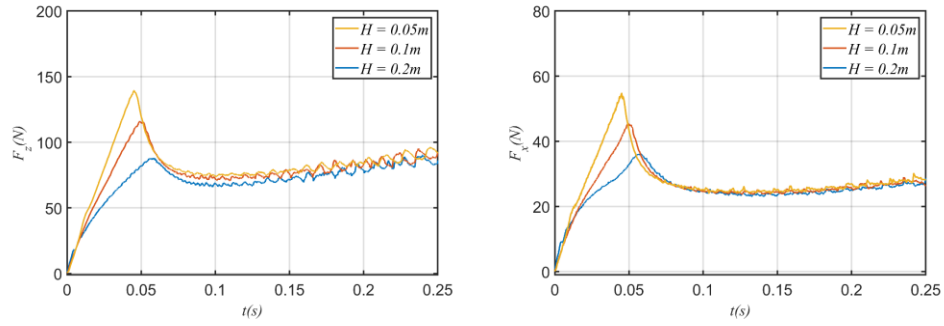


Fig. 22 Total force for wave entry of an asymmetric wedge of  $\gamma_1 = 30^\circ, \gamma_2 = 60^\circ$

with different wave heights.

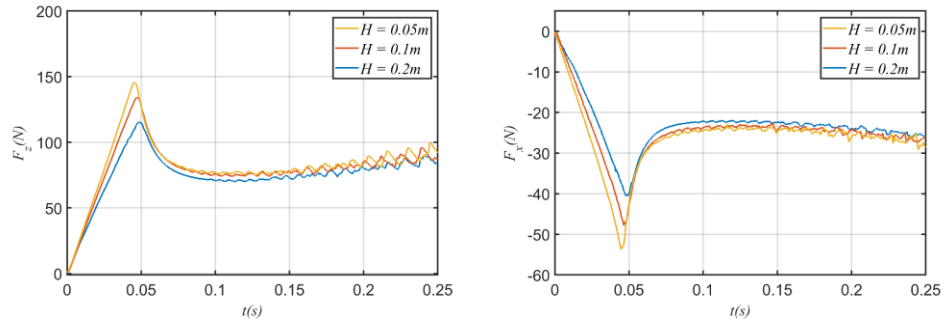


Fig. 23 Total force for wave entry of an asymmetric wedge of  $\gamma_1 = 60^\circ, \gamma_2 = 30^\circ$

with different wave heights.

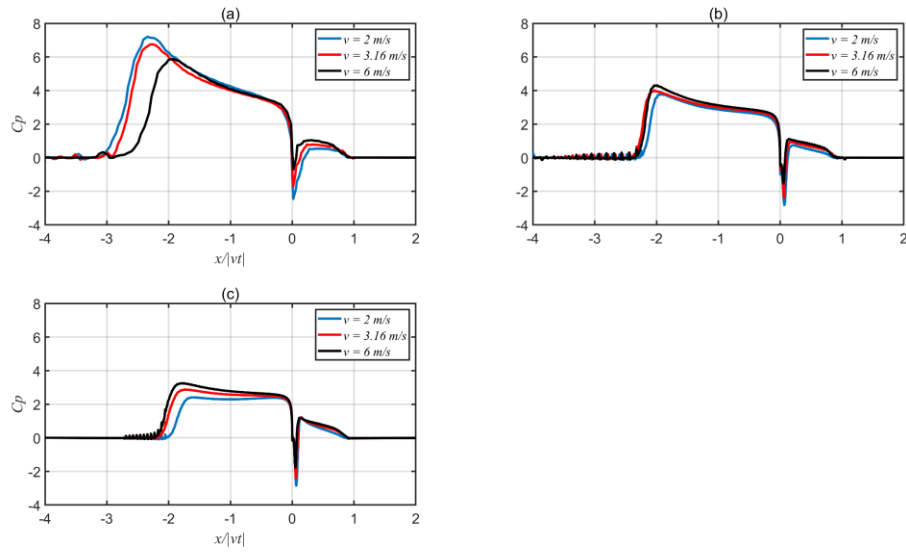


Fig. 24. Pressure distribution for wave entry of an asymmetric wedge of  $\gamma_1 = 30^\circ$ ,  $\gamma_2 = 60^\circ$  with different velocities. (a)  $s = 0.004 \cdot 3.16 \text{ m}$ , (b)  $s = 0.02 \cdot 3.16 \text{ m}$ , (c)  $s = 0.04 \cdot 3.16 \text{ m}$ .

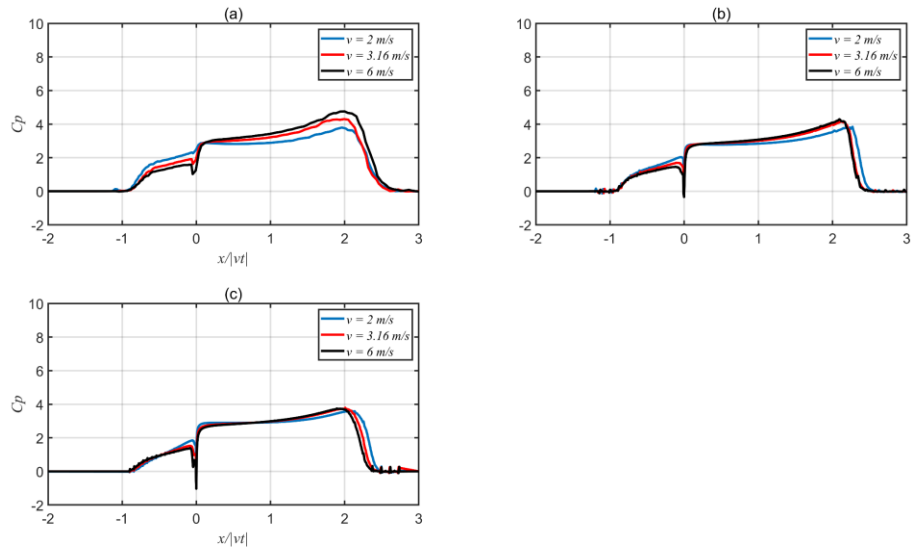


Fig. 25. Pressure distribution for wave entry of an asymmetric wedge of  $\gamma_1 = 60^\circ$ ,  $\gamma_2 = 30^\circ$  with different velocities. (a)  $s = 0.004 \cdot 3.16 \text{ m}$ , (b)  $s = 0.02 \cdot 3.16 \text{ m}$ , (c)  $s = 0.04 \cdot 3.16 \text{ m}$ .

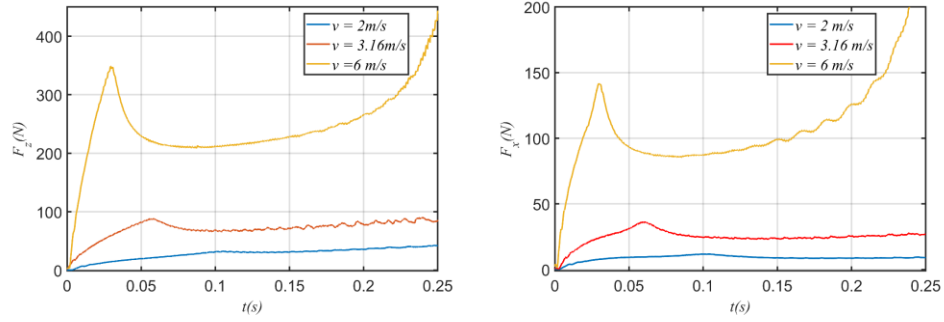


Fig. 26 Total force for wave entry of an asymmetric wedge of  $\gamma_1 = 30^\circ, \gamma_2 = 60^\circ$  with

different velocities.

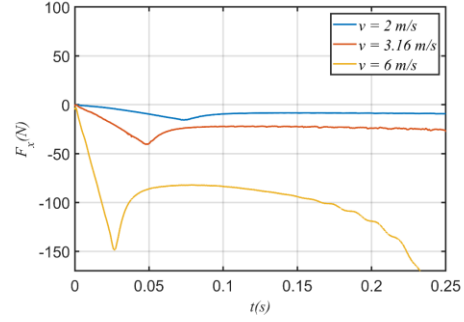
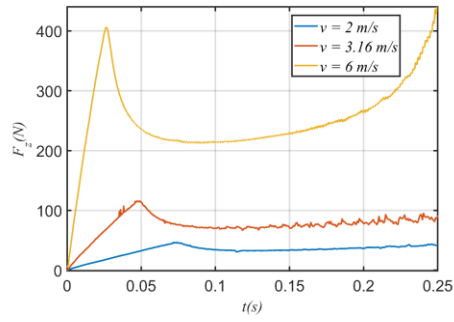


Fig. 27 Total force for wave entry of an asymmetric wedge of  $\gamma_1 = 60^\circ, \gamma_2 = 30^\circ$

with different velocities.



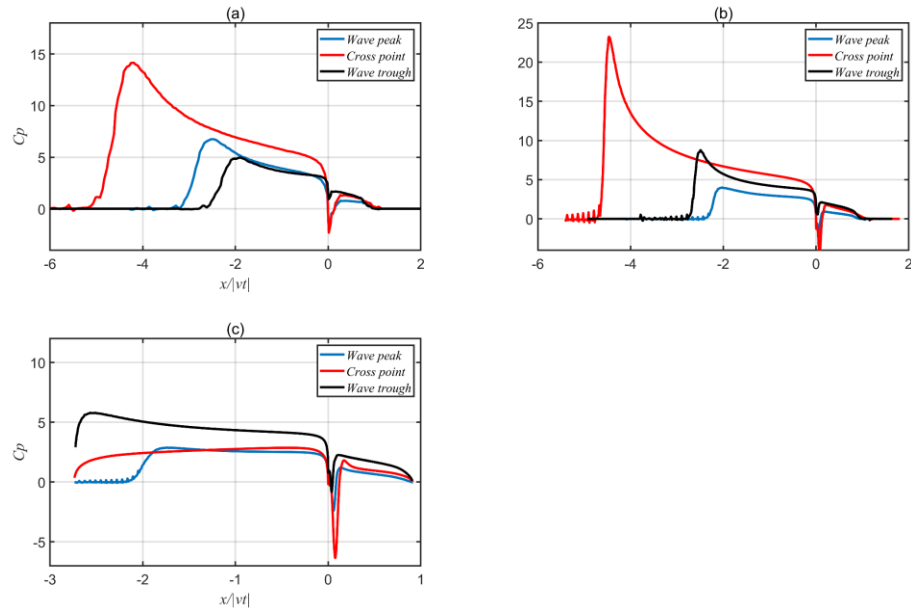


Fig. 28. Pressure distribution for wave entry of an asymmetric wedge of  $\gamma_1 = 30^\circ$ ,  $\gamma_2 = 60^\circ$  with different entry locations. (a)  $t = 0.004s$ , (b)  $t = 0.02s$ , (c)  $t = 0.04s$ .

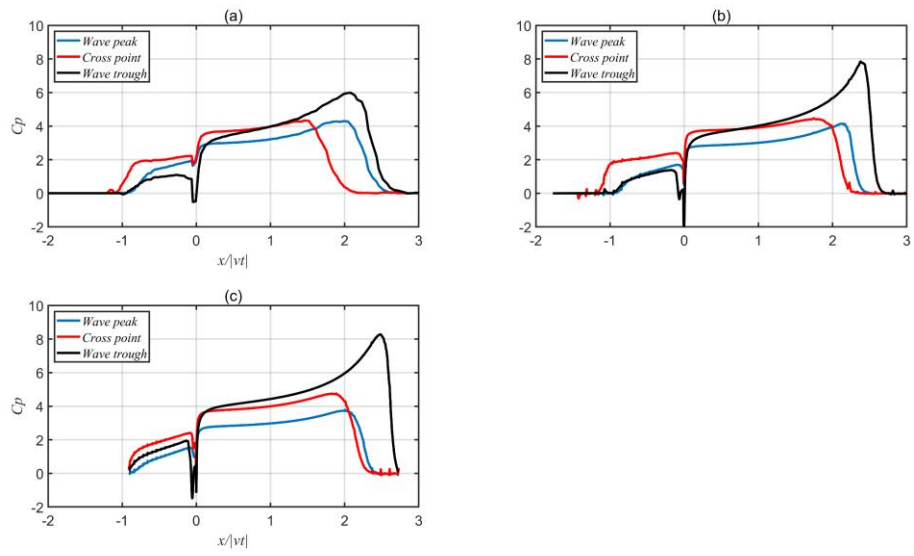


Fig. 29. Pressure distribution for wave entry of an asymmetric wedge of  $\gamma_1 = 60^\circ$ ,  $\gamma_2 = 30^\circ$  with different entry locations. (a)  $t = 0.004s$ , (b)  $t = 0.02s$ , (c)  $t = 0.04s$ .

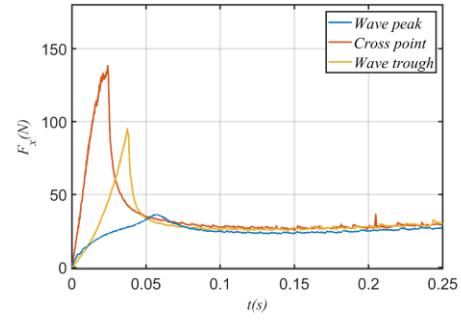
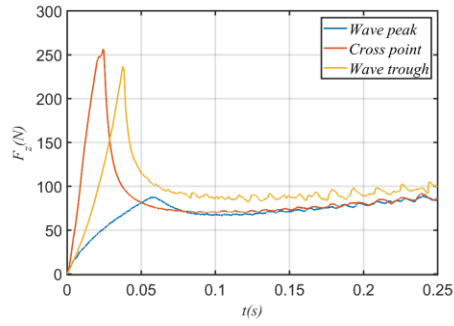


Fig. 30 Total force for wave entry of an asymmetric wedge of  $\gamma_1 = 30^\circ, \gamma_2 = 60^\circ$

with different entry locations.

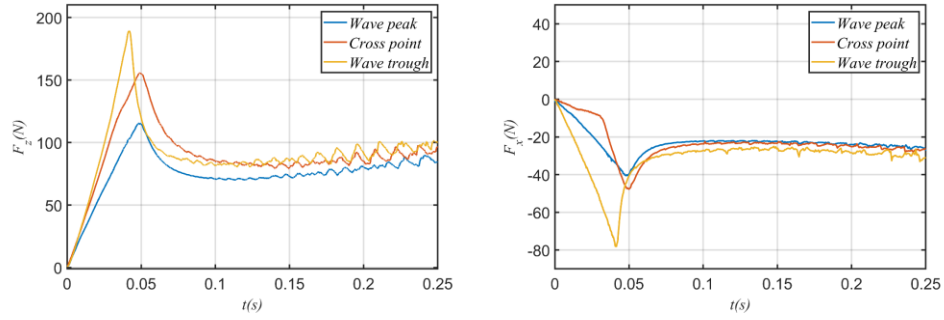


Fig. 31 Total force for wave entry of an asymmetric wedge of  $\gamma_1 = 60^\circ, \gamma_2 = 30^\circ$

with different entry locations.